

The Dynamical Cluster Approximation: A New Technique for Simulations of Strongly Correlated Electron Systems

S. Moukouri, C. Huscroft, and M. Jarrell

University of Cincinnati, Cincinnati OH 45221, USA

Abstract. We present the algorithmic details of the dynamical cluster approximation (DCA) algorithm. The DCA is a fully-causal approach which systematically restores non-local correlations to the dynamical mean field approximation (DMFA). The DCA is in the thermodynamic limit and becomes exact for an infinite cluster size, while reducing to the DMFA for a cluster size of unity. Using the one-dimensional Hubbard Model as a non-trivial test of the method, we systematically compare the results of a quantum Monte Carlo (QMC) based DCA with those obtained by finite-size QMC simulations (FSS). We find that the single-particle Green function and the self-energy of the DCA and FSS approach the same limit as the system size is increased, but from complimentary directions. The utility of the DCA in addressing problems that have not been resolved by FSS is demonstrated.

1 Introduction

One of the most active subfields in condensed matter theory is the development of new algorithms to simulate the many-body problem. This interest is motivated by various physical phenomena, including high temperature superconductivity, magnetism, heavy fermions and the rich phenomenology occurring in quasi-one dimensional compounds. In the last few years, important progress has been made. Well-controlled results have been obtained by exact diagonalization and quantum Monte Carlo methods (QMC)[1]. However, these algorithms suffer from a common limitation in that the number of degrees of freedom grows rapidly with the lattice size. As a consequence, the calculations are restricted to relatively small systems. In most cases, the limited size of the system prohibits the study of the low-energy physics of these models.

Recently, another route to quantum simulations has been proposed. Following Metzner and Vollhardt[5] and Müller-Hartmann[7] who showed that in the limit of infinite dimensions, the many-body problem becomes purely local, a mapping to a self-consistent Anderson impurity problem was performed [13][12]. The availability of many techniques to solve the Anderson impurity Hamiltonian has led to a dramatic burst activity. However, when applied to systems in two or three dimensions this self-consistent approximation, referred to as the dynamical mean field approximation (DMFA), displays some limitations. Due to its local nature, the DMFA neglects spatial fluctuations

which are essential when the order parameter is non-local. This is the case in the cuprate or heavy fermion superconductors. Methods that at least include short-range spatial fluctuations are currently the object of intensive research. These techniques map the lattice problem to a self-consistently embedded finite-sized cluster, instead of a single impurity as in DMFA.

The most promising of these techniques is the dynamical cluster approximation (DCA) [2][3][4]. The key idea of the DCA is to use the irreducible quantities (self energy, irreducible vertices) of the embedded cluster as an approximation for the lattice quantities. These irreducible quantities are then applied to construct the lattice reducible quantities such as the Green function or susceptibilities in the different channels. The cluster problem is solved by using a generalization of the Hirsch-Fye quantum Monte Carlo (QMC) method.

In this paper, we discuss the novelty and the new perspectives offered by the DCA. We use the one-dimensional Hubbard model as a test case. We analyze the convergence of the DCA in comparison to that of the usual finite systems simulations (FSS). The choice of a one-dimensional model is particularly instructive. A success of the DCA in 1D, where quantum fluctuations are the strongest, means that the method can work in any dimension. We show that the DCA produces results which are complementary to those obtained by FSS.

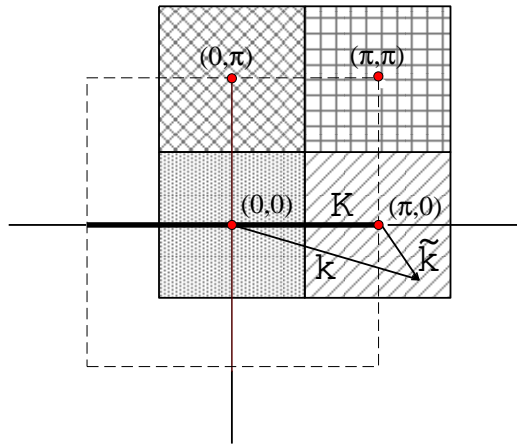


Fig. 1. $N_c = 4$ cluster cells (shown by different fill patterns) that partition the first Brillouin Zone (dashed line). Each cell is centered on a cluster momentum \mathbf{K} (filled circles). To construct the DCA cluster, we map a generic momentum in the zone such as \mathbf{k} to the nearest cluster point $\mathbf{K} = \mathbf{M}(\mathbf{k})$ so that $\tilde{\mathbf{k}} = \mathbf{k} - \mathbf{K}$ remains in the cell around \mathbf{K} .

2 The Dynamical Cluster Approximation

2.1 Formalism

The DCA is based on the assumption that the lattice self energy is weakly momentum dependent. This is equivalent to assuming that the dynamical intersite correlations have a short spatial range $< L/2$ where L is the linear dimension of the cluster. Then, according to Nyquist's sampling theorem[6], to reproduce these correlations in the self energy, we only need to sample the reciprocal space at intervals of $\Delta k \approx 2\pi/L$. Therefore, we could approximate $G(\mathbf{K} + \tilde{\mathbf{k}})$ by $G(\mathbf{K})$ within the cell of size $(\pi/L)^D$ (see, Fig. 1) centered on the cluster momentum \mathbf{K} (wherever feasible, we suppress the frequency labels) and use this Green function to calculate the self energy. Knowledge of these Green functions on a finer scale in momentum is unnecessary, and may be discarded to reduce the complexity of the problem. Thus the cluster self energy can be constructed from the *coarse-grained average* of the single-particle Green function within the cell centered on the cluster momenta:

$$\bar{G}(\mathbf{K}) \equiv \frac{N_c}{N} \sum_{\tilde{\mathbf{k}}} G(\mathbf{K} + \tilde{\mathbf{k}}) \quad , \quad (1)$$

where N is the number of points of the lattice, N_c is the number of cells in the cluster, and the $\tilde{\mathbf{k}}$ summation runs over the momenta of the cell about the cluster momentum \mathbf{K} (see, Fig. 1). For short distances $r < L/2$ the Fourier transform of the Green function $\bar{G}(r) \approx G(r) + \mathcal{O}((r\Delta k)^2)$, so that short ranged correlations are reflected in the irreducible quantities constructed from \bar{G} ; whereas, longer ranged correlations $r > L/2$ are cut off by the finite size of the cluster.[2]

This coarse graining procedure and the relationship of the DCA to the DMFA is illustrated by a microscopic diagrammatic derivation of the DCA. For Hubbard-like models, the properties of the bare vertex are completely characterized by the Laue function Δ which expresses the momentum conservation at each vertex. In a conventional diagrammatic approach

$$\Delta(\mathbf{k}_1, \mathbf{k}_2, \mathbf{k}_3, \mathbf{k}_4) = \sum_{\mathbf{r}} \exp[i\mathbf{r} \cdot (\mathbf{k}_1 - \mathbf{k}_2 + \mathbf{k}_3 - \mathbf{k}_4)] = N\delta_{\mathbf{k}_1 + \mathbf{k}_2, \mathbf{k}_3 + \mathbf{k}_4} \quad (2)$$

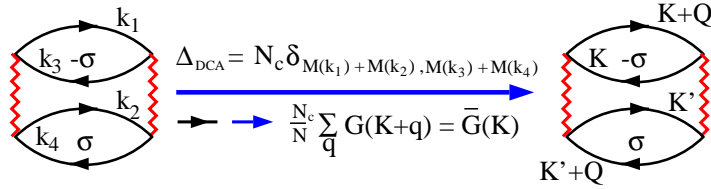


Fig. 2. The DCA choice of the Laue function Eq. 4 leads to the replacement of the lattice propagators $G(\mathbf{k}_1), G(\mathbf{k}_2), \dots$ by coarse grained propagators $\bar{G}(\mathbf{K}), \bar{G}(\mathbf{K}'), \dots$ (Eq. 1) in the internal legs of Φ_{DCA} , illustrated for a second order diagram.

where \mathbf{k}_1 and \mathbf{k}_2 (\mathbf{k}_3 and \mathbf{k}_4) are the momenta entering (leaving) each vertex through its legs of G . However as $D \rightarrow \infty$ Müller-Hartmann showed that the Laue function reduces to[7]

$$\Delta_{D \rightarrow \infty}(\mathbf{k}_1, \mathbf{k}_2, \mathbf{k}_3, \mathbf{k}_4) = 1 + \mathcal{O}(1/D) \quad . \quad (3)$$

The DMFA assumes the same Laue function, $\Delta_{DMFA}(\mathbf{k}_1, \mathbf{k}_2, \mathbf{k}_3, \mathbf{k}_4) = 1$, even in the context of finite dimensions. Thus, the conservation of momentum at internal vertices is neglected. Therefore we may freely sum over the internal momenta at each vertex in the generating functional Φ_{DMFA} . This leads to a collapse of the momentum dependent contributions to the functional Φ_{DMFA} and only local terms remain.

The DCA systematically restores the momentum conservation at internal vertices. The Brillouin-zone is divided into $N_c = L^D$ cells of size $(2\pi/L)^D$. Each cell is represented by a cluster momentum \mathbf{K} in the center of the cell. We require that momentum conservation is (partially) observed for momentum transfers between cells, i.e., for momentum transfers larger than $\Delta k = 2\pi/L$, but neglected for momentum transfers within a cell, i.e., less than Δk . This requirement can be established by using the Laue function [2]

$$\Delta_{DCA}(\mathbf{k}_1, \mathbf{k}_2, \mathbf{k}_3, \mathbf{k}_4) = N_c \delta_{\mathbf{M}(\mathbf{k}_1)+\mathbf{M}(\mathbf{k}_3), \mathbf{M}(\mathbf{k}_2)+\mathbf{M}(\mathbf{k}_4)} \quad , \quad (4)$$

where $\mathbf{M}(\mathbf{k})$ is a function which maps \mathbf{k} onto the momentum label \mathbf{K} of the cell containing \mathbf{k} (see, Fig. 1). With this choice of the Laue function the momenta of each internal leg may be freely summed over the cell. This is illustrated for the second-order term in the generating functional in Fig. 2. Thus, each internal leg $G(\mathbf{k}_1)$ in a diagram is replaced by the coarse-grained Green function $\bar{G}(\mathbf{M}(\mathbf{k}_1))$, defined by Eq. 1. The diagrammatic sequences for the generating functional and its derivatives are unchanged; however, the complexity of the problem is greatly reduced since $N_c \ll N$. We showed previously[2,4] that the DCA estimate of the lattice free-energy is minimized by the approximation $\Sigma(\mathbf{k}) \approx \bar{\Sigma}(\mathbf{M}(\mathbf{k})) + \mathcal{O}(\Delta k^2)$, where $\delta\Phi_{DCA}/\delta\bar{G} = \bar{\Sigma}$.

One advantage of the DCA over other attempts to build self-consistent cluster techniques is that the DCA is fully causal. The spectral weight is conserved and the imaginary part of the single-particle retarded Green function and self-energy are negative definite. Hettler et al. used a geometric argument to derive a rigorous proof of the causality of the DCA [2].

2.2 One and two-particle quantities

In the DMFA, after convergence, the local Green function of the lattice is identical to that of the impurity model. Though in the DCA, the coarse-grained Green function $\bar{G}(K)$ is equal to the cluster Green function, this quantity is not used as an approximation to the true lattice Green function $G(K)$. The correct procedure to calculate the lattice physical quantities within the DCA is to approximate the lattice irreducible quantities with those

of the cluster. The lattice reducible quantities are then deduced from the irreducible. In order to completely understand the DCA formalism, one must understand why reducible and irreducible quantities are treated differently. Consider a screened particle (a quasiparticle) propagating through the system, as pictured in Fig. 3. Here, we will assume that the screening length, e.g., due to Thomas-Fermi screening, r_{TF} is short. This screening cloud is described by the single-particle self energy $\Sigma(\mathbf{k}, \omega)$ which itself may be considered a functional of the interaction strength U and the single-particle propagator $G(\mathbf{k}, \omega)$. The different screening processes are described perturbatively by a sum of self energy diagrams. Due to the short screening length, the propagators which describe these processes need only be accurate for lengths $< r_{TF}$. From the Fourier uncertainty principle, we know that the propagators at short lengths may be accurately described by a coarse sampling of the reciprocal space, with sampling rate $\Delta k = \pi/r_{TF}$. On the other hand, the phase accumulated as the particle propagates through the system is described by the Fourier transform of the single-particle Green function. Since this accumulated phase is crucial in the description of the quantum dynamics it is important that $G(r)$ remain accurate at long length scales, so it should not be coarse-grained as described above. However it may be constructed from the approximate self energy. Hence, the lattice Green function is given by,

$$G(\mathbf{k}) = \frac{1}{i\omega_n - \epsilon_{\mathbf{k}} - \Sigma(M(\mathbf{k}))} \quad . \quad (5)$$

A similar procedure is used to construct the two-particle quantities needed to determine the phase diagram or the nature of the dominant fluctuations that can eventually destroy the single-particle quasi-particle. They are computed in the same fashion as the single-particle ones. The irreducible vertex Γ is the analogue of the self energy for two-particle quantities. In a general many-body theory, Γ has four entries describing the states of a pair before and after the interaction,

$$\Gamma = \Gamma(k_1, k_2, k_3, k_4) \quad . \quad (6)$$

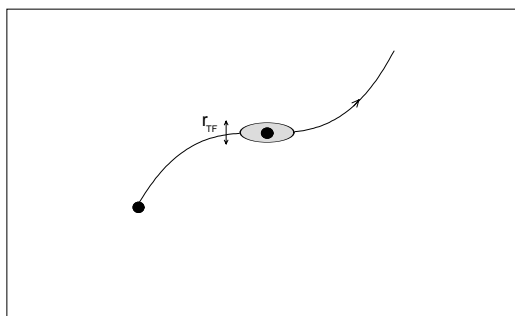


Fig. 3. Motion of a particle with its screening cloud

The diagonalization of Γ in spin space reduces to the usual density and magnetic fluctuations in the particle-hole channel or singlet and triplet fluctuation in the particle-particle channel. For the sake of simplicity, we will use a generic notation below which describes any one of these four fluctuations. Momentum conservation ensures that there are only three independent momenta, $\Gamma = \Gamma(q, k, k')$. We assume, as for the self energy, that the irreducible vertex $\Gamma = \frac{\delta \Sigma}{\delta G}$ is weakly momentum dependent. Hence, this quantity is equated to the corresponding cluster quantity within a cell surrounding the cluster momentum for each momentum involved in $\Gamma(q, k, k')$. This gives,

$$\Gamma_{\mathbf{Q}+\tilde{\mathbf{q}}}(\mathbf{K} + \tilde{\mathbf{k}}, \mathbf{K}' + \tilde{\mathbf{k}}') = \Gamma_{\mathbf{Q}}(\mathbf{K}, \mathbf{K}') \quad . \quad (7)$$

The calculation procedure of the reducible two-particle quantities from the irreducible vertex Γ will now be described. The QMC cluster susceptibility

$$\chi_c(Q, K, K') = \langle c_{K+Q}^\dagger(\tau) c_{K'-Q}(\tau') c_K^\dagger(0) c_{K'}(0) \rangle \quad , \quad (8)$$

calculated in the appropriate channel is the analogue of the single-particle Green function G_c . But this quantity is different from the coarse grained susceptibility $\bar{\chi}$,

$$\bar{\chi}_{\mathbf{Q}+\tilde{\mathbf{q}}}(\mathbf{K}, \mathbf{K}') = \frac{N_c^2}{N^2} \sum_{\tilde{\mathbf{k}}, \tilde{\mathbf{k}}'} \chi_{\mathbf{Q}+\tilde{\mathbf{q}}}(\mathbf{K} + \tilde{\mathbf{k}}, \mathbf{K}' + \tilde{\mathbf{k}}') \quad , \quad (9)$$

where χ is the lattice susceptibility. In the DCA, $\bar{\chi}$ and χ_c are both related to Γ through the reduced Bethe-Salpeter equation,

$$\chi_{\mathbf{Q}+\tilde{\mathbf{q}}}^\alpha = \chi_{\mathbf{Q}+\tilde{\mathbf{q}}}^{0\alpha} + \chi_{\mathbf{Q}+\tilde{\mathbf{q}}}^{0\alpha} \Gamma_Q \chi_{\mathbf{Q}+\tilde{\mathbf{q}}}^\alpha \quad , \quad (10)$$

χ^α represents either χ_c or $\bar{\chi}$. $\bar{\chi}_{\mathbf{Q}+\tilde{\mathbf{q}}}^0$ is obtained from the single-particle Green function as follows,

$$\bar{\chi}_{\mathbf{Q}+\tilde{\mathbf{q}}}^0 = \delta_{\mathbf{K}, \mathbf{K}'} \frac{N_c^2}{N} \sum_{\tilde{\mathbf{k}}} G(\mathbf{K} + \tilde{\mathbf{k}}) G(\mathbf{K} + \tilde{\mathbf{k}} + \mathbf{Q} + \tilde{\mathbf{q}}) \quad . \quad (11)$$

In Eq. 10 above, the sum is restricted to cluster momenta. This constitutes a significant simplification of the lattice problem which may be otherwise intractable. Yet, as the cluster size increases, the full solution of this reduced Bethe-Salpeter equation may require a significant amount of computer storage and CPU time. We thus restrict ourselves to momenta \mathbf{Q} where a given type of fluctuation is likely to diverge, i.e., $\mathbf{Q} = 0$ for the density, singlet or $\mathbf{Q} = (\pi, \pi)$ magnetic fluctuations. The inversion of each of the two equations then yields

$$\bar{\chi}^{-1} = \chi_c^{-1} - \chi_c^{0-1} + \bar{\chi}^{0-1} \quad . \quad (12)$$

The charge (ch) and spin (sp) susceptibilities $\tilde{\chi}_{ch,sp}$ are deduced from $\bar{\chi}$

$$\tilde{\chi}_{ch,sp}(\mathbf{q}, i\omega_n) = \frac{(k_B T)^2}{N_c^2} \sum_{\mathbf{K} \mathbf{K}' m m' \sigma \sigma'} \lambda_{\sigma \sigma'} \bar{\chi}_{\mathbf{q}}(\mathbf{K}, i\omega_m; \mathbf{K}', i\omega_{m'}) \quad , \quad (13)$$

where $\lambda_{\sigma \sigma'} = 1$ for the charge channel and $\lambda_{\sigma \sigma'} = \sigma \sigma'$ for the spin channel.

2.3 The DCA algorithm

Table 1. Steps of the DCA algorithm

0. set $\Sigma = 0$
1. calculate the coarse-grained Green function \bar{G}
2. calculate $\mathcal{G}^{-1} = \bar{G}^{-1} + \Sigma$
3. using Hirsch-Fye calculate the cluster Green function G_c
4. compute a new estimate of $\Sigma = \mathcal{G}^{-1} - G_c^{-1}$
5. repeat 1-4 until Σ converges
6. accumulate bins of measurements on G_c, χ_c
7. calculate the lattice Green function G , spectral weight, susceptibilities...

The DCA iteration procedure is set forth in Table 1. It is started by setting the initial self energy to zero. This self energy is then used to compute the coarse-grained Green function $\bar{G}(\mathbf{K})$. The latter is used to compute the host Green function $\mathcal{G}(\mathbf{K})^{-1} = \bar{G}(\mathbf{K})^{-1} + \Sigma(\mathbf{K})$ which must be introduced to avoid over-counting diagrams. \mathcal{G} serves as the input to the QMC simulation to yield a new estimate of the cluster self energy. The procedure is repeated until Σ converges. This typically happens in less than ten iterations. The number of iterations decreases when N_c increases since the coupling to the host is smaller for larger clusters ($\Gamma \approx \mathcal{O}(1/N_c)$) [4]. The convergence test is made on the ratio ρ ,

$$\rho = \frac{|\sum_n (\Sigma_{new}(i\omega_n) - \Sigma_{old}(i\omega_n))|}{|\sum_n \Sigma_{old}(i\omega_n)|} . \quad (14)$$

Once convergence is reached, the remaining single and two-particle measurements are made in a final QMC iteration. As in a usual QMC simulation, bins of measurements are accumulated as discussed in the next section. One should, however, bear in mind that these measurements are performed with \bar{G} instead of the true lattice Green function G . Hence, the determination of the lattice quantities requires an additional step in which the coarse-graining equation is inverted. This is done in a separate program.

3 The Hirsch-Fye QMC algorithm

The cluster problem is solved using one of the available finite system techniques. The Hirsch-Fye (HF) algorithm [8], which was originally proposed for impurity problems, is easily adapted to embedded cluster simulations as required in the DCA. We recall here the main steps of its derivation. For details we refer the reader to the original Hirsch and Fye paper or the review by Georges *et al* [12]. One starts by writing the partition function in the Grand-canonical ensemble,

$$Z = \text{Tr} e^{-\beta(H - \mu N)} . \quad (15)$$

Then the exponential is broken up into N_τ imaginary-time slices and the Trotter approximation is employed to separate the kinetic, K , and interacting, V , parts of the Hamiltonian H ,

$$e^{[-\beta(H-\mu N)]} = \prod_{l=1}^{N_\tau} e^{[-\Delta\tau(K_l+V_l)]} \approx \prod_{l=1}^{N_\tau} e^{-\Delta\tau K_l} e^{-\Delta\tau V_l} \quad , \quad (16)$$

where $N_\tau \Delta\tau = \beta$. The error made during the last step is of the order of $(\Delta\tau)^2$. The next step is to replace this interacting problem by one consisting of non-interacting particles moving in a fluctuating field x_α , where the index α stands for space and imaginary-time coordinates. This is done by employing the Hirsch-Hubbard-Stratonovitch (HHS) transformation,

$$e^{[-\Delta\tau U(n_{\alpha\uparrow}-\frac{1}{2})(n_{\alpha\downarrow}-\frac{1}{2})]} = \frac{e^{[-\Delta\tau \frac{U}{4}]} }{2} \sum_{x_\alpha=\pm 1} e^{[\lambda x_\alpha(n_{\alpha\uparrow}-n_{\alpha\downarrow})]} \quad . \quad (17)$$

After the HHS transformation, the quartic operator V becomes quadratic like K . In this new form a trace over the fermion degrees of freedom can be exactly performed. It yields,

$$Z = \sum_{x_\alpha} \prod_{\sigma=\uparrow\downarrow} \det[(G_c^\sigma(x_\alpha))^{-1}] \quad , \quad (18)$$

where the sum is over the configurations of HHS fields x_α . The dimension of the Green function matrix G_c^σ is $(N_\tau \times N_c)^2$. It is at this point that the HF algorithm differs from the Blaukenbecker-Sugar-Scalapino (BSS) algorithm[11]. In the HF, the simulation deals directly with the matrix G_c^σ . In the BSS the locality of the action in time is used to reduce the matrix-size in the simulation. However, this cannot be done when action is non-local in time, as in this case where the cluster is coupled to a host.

The algorithm starts with an initial Green function $G_c = \mathcal{G}$ and a corresponding initial configuration of the fields x_α . It then sweeps the space-time lattice by proposing flips in the fields $x_\alpha \rightarrow x'_\alpha = -x_\alpha$. The heat-bath or the Metropolis algorithm is used to determine if the change will be accepted. The probability $P(x_\alpha)$ of the configuration x_α is proportional to $\prod_{\sigma=\uparrow\downarrow} \det[(G_c^\sigma(x_\alpha))^{-1}]$. The transition probability is

$$R = \frac{\prod_{\sigma=\uparrow\downarrow} \det[(G_c'^\sigma(x_\alpha))^{-1}]}{\prod_{\sigma=\uparrow\downarrow} \det[(G_c^\sigma(x_\alpha))^{-1}]} \quad . \quad (19)$$

If the new configuration is accepted, the Green function is updated by using the relation

$$G_c'^\sigma{}_{i,j} = G_c^\sigma{}_{i,j} + \frac{(G_c^\sigma{}_{j,k} - \delta_{i,k})e^{[-\lambda\sigma(V-V')]} }{1 + (1 - G_c^\sigma{}_{k,k})(e^{-\lambda\sigma(V-V')} - 1)} G_c^\sigma{}_{k,j} \quad . \quad (20)$$

The initial field configuration is chosen with all $x_\alpha = 0$. The above equation is then used to construct a physically realistic field configuration (i.e.,

$x_\alpha = 1$ for all fields). The system is then warmed up by sequentially stepping through the space-time lattice, proposing changes at each space-time site $x_\alpha \rightarrow -x_\alpha$. The change is accepted if the transition probability is greater than a random number between 0 and 1. Typically, the warm up phase lasts for about a hundred space-time sweeps before measurements begin. It is necessary to perform a few complete space-time sweeps in order to produce more-or-less independent measurements. For clusters, the Hirsch-Fye algorithm is very efficient and stable at low temperatures.

4 Numerical Aspects

One difficulty encountered with the DCA algorithm is that a reliable transform from imaginary-time quantities, in the QMC part, to Matsubara frequencies, in the QMC part, to Matsubara frequencies, for the coarse-graining part is needed. A careful treatment of the frequency summation or the imaginary-time integration is crucial in order to ensure the accuracy and the stability of the algorithm and to maintain the correct high-frequency behavior of the Green functions. We need to evaluate the following integral

$$G_c(\mathbf{K}, i\omega_n) = \int_0^\beta d\tau e^{i\omega\tau} G_c(\mathbf{K}, \tau) \quad . \quad (21)$$

But from the QMC, we know the function $G_c(\mathbf{K}, \tau)$ only at a discrete subset of the interval $[0, \beta]$. As it may be readily seen by discretizing the above equation, the estimation of $G_c(\mathbf{K}, i\omega_n)$ becomes inaccurate at high-frequencies.

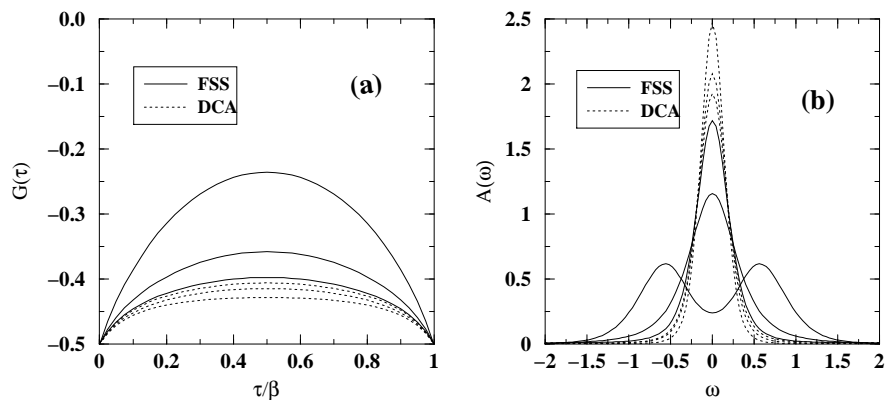


Fig. 4. (a) Imaginary-time Green function at the Fermi point for $U = 2$, $\beta = 5$ for FSS (solid lines) for $N_c=4,8,16$ (from top to bottom) and for DCA (dotted lines) for $N_c=4,8,12$ (from bottom to top). (b) The corresponding spectral weights for FSS (solid lines) $N_c=4,8,12$ (increasing value at $\omega = 0$) and DCA (dotted lines) $N_c=4,8,12$ (decreasing value at $\omega = 0$).

This is formalized by Nyquist's theorem which tells us that above the frequency $\omega_c = \frac{\pi}{\Delta\tau}$ unpredictable results are produced by conventional quadrature techniques. A straightforward way to cure this problem may be to increase the size of the set of τ -points where the Green function is evaluated. But, this renders the QMC simulation rapidly intractable as seen in the previous section. A much more economic way to avoid the problem is to use an approximate method that is asymptotically exact.

Second-order perturbation theory is enough to obtain the correct asymptotic behavior. For instance, we compute the Matsubara-frequency Green function from the imaginary-time QMC Green function as follows [10]

$$G_c(\mathbf{K}, i\omega_n) = G_{cpt}(\mathbf{K}, i\omega_n) + \int_0^\beta d\tau e^{i\omega\tau} (G_c(\mathbf{K}, \tau) - G_{cpt}(\mathbf{K}, \tau)) \quad . \quad (22)$$

The integral is computed by first splining the difference $G_c(\mathbf{K}, \tau) - G_{cpt}(\mathbf{K}, \tau)$, and then integrating the spline (a technique often called oversampling).

Once convergence is reached, $\bar{G} = G_c$, and the QMC Green function G_c may be analytically continued using the Maximum-entropy method (MEM). Unfortunately, there is no reliable way to perform the direct analytic continuation of $\Sigma(\mathbf{K})$. Padé approximants lead to very unstable spectra because of the QMC statistical noise contained in $\Sigma(\mathbf{K})$. The binned imaginary-time Green function data accumulated from the cluster calculation must be used to obtain lattice spectra from which $\Sigma(\mathbf{K})$ may be deduced. To obtain the self-energy and spectral-weight function $A(\mathbf{k}, \omega)$ of the lattice in real frequencies, we first compute the cluster spectral-weight $\bar{A}(\mathbf{K}, \omega)$ by using the Maximum

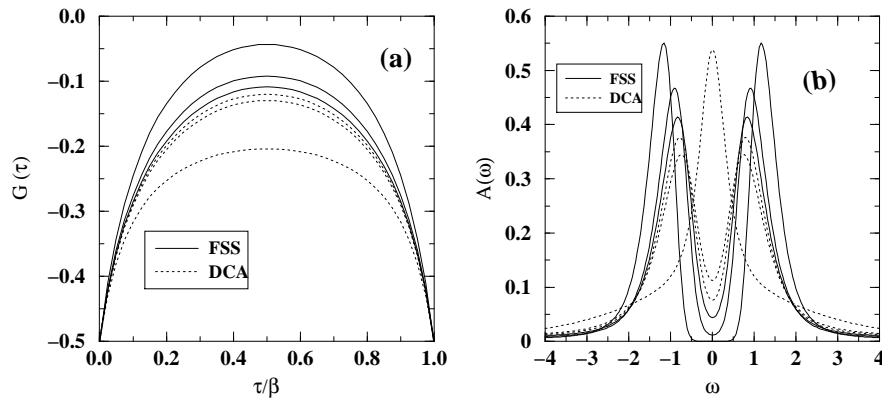


Fig. 5. (a) Imaginary-time Green function at the Fermi point for $U = 4$, $\beta = 5$ for FSS (solid lines) for $N_c = 4, 8, 16$ (from top to bottom) and for DCA (dotted lines) for $N_c = 4, 8, 12$ (from bottom to top). (b) The corresponding spectral weights for FSS (solid lines) $N_c = 4, 8, 12$ (increasing value at $\omega = 0$) and DCA (dotted lines) $N_c = 4, 8, 12$ (decreasing value at $\omega = 0$).

entropy method [9] for the inversion of the following integral equation

$$\bar{G}(\mathbf{K}, \tau) = \int d\omega \frac{e^{-\omega\tau}}{1 + e^{-\beta\omega}} \bar{A}(\mathbf{K}, \omega) \quad , \quad (23)$$

where $\bar{G}(\mathbf{K}, \tau)$ is the imaginary-time Green function obtained from the QMC simulation of the cluster. From $\bar{A}(\mathbf{K}, \omega)$, we obtain the coarse-grained Green function in real frequencies by Kramers-Krönig analysis. Finally, we solve equation (1) to obtain $\Sigma(\mathbf{K}, \omega)$ from $\bar{G}(\mathbf{K}, \omega)$.

5 Example: the One-dimensional Hubbard Model

In this section, we apply the DCA to the one-dimensional Hubbard model at half-filling. Such a test is interesting for several reasons. First, this test will help verify whether recent applications of the DCA in two dimensions are reasonably anticipated to be accurate. In one dimension, quantum fluctuations are stronger than in higher dimensions. Hence, one intuitively expects the DCA to be less efficient in one than in higher dimensions. So, if the DCA accurately captures the physics in one dimension, then it is highly likely to capture the physics of two and three dimensions accurately. Second, although the DCA is known to become exact in the limit of an infinite cluster, an extensive, systematic analysis of the convergence of the DCA has not yet been

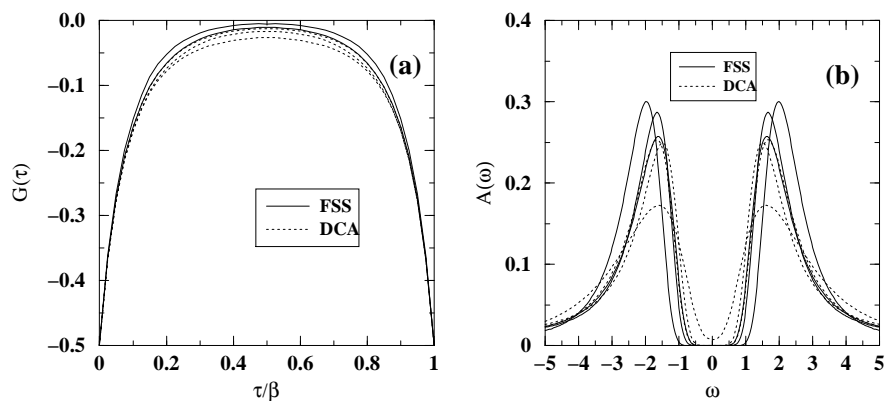


Fig. 6. (a) Imaginary-time Green function at the Fermi point for $U = 6$, $\beta = 5$ for FSS (solid lines) for $N_c=4, 8, 16$ (from top to bottom) and for DCA (dotted lines) for $N_c=4, 8, 12$ (from bottom to top). (b) The corresponding spectral weights for FSS (solid lines) $N_c=4, 8, 12$ (broad to narrow gap) and DCA (dotted lines) $N_c=4, 8, 12$ (narrow to broad gap). Note that once a gap opens in the spectral function, the maximum-entropy analytic continuation procedure becomes unreliable.[9] This unreliability is believed to be the source of the non-systematic nature of the peaks in the spectral functions. Although unreliable for fine structure, the qualitative feature of the existence of a gap is accurately depicted in this figure.

performed. Finally, it is desirable to illustrate differences between the DCA and a widely-applied FSS method in a well-studied, non-trivial problem.

The 1D Hubbard Hamiltonian is widely accepted as the most relevant model in the high temperature regime of the 1D organic materials, for which a significant volume of experimental data is available. It is well-studied and provides a non-trivial test of the DCA. The Hubbard Hamiltonian reads:

$$H = -t \sum_i (c_{i\sigma}^+ c_{i+1\sigma} + hc) + U \sum_i n_{i\uparrow} n_{i\downarrow} \quad , \quad (24)$$

with a next-nearest-neighbor hopping and an on-site repulsion t and U , respectively, on a one-dimensional lattice. We set $t = 1$ throughout this study and measure all energies in terms of t . We work at half-filling, where the QMC is free of the fermion sign problem, eliminating one possible source of errors in both the FSS and the DCA. This allows us to easily isolate actual discrepancies between the FSS and the DCA. Although the 1D Hubbard model can be solved exactly, the FSS QMC is currently the only reliable method used to compute finite temperature dynamics.

We now turn to a comparison of the imaginary-time Green function at the Fermi-point of the DCA and of FSS. We see that the two methods converge differently to the exact result. The quantity

$$G(k_F, \beta/2) = \frac{1}{2} \int d\omega \frac{A(k_F, \omega)}{\cosh(\frac{\beta\omega}{2})} \quad , \quad (25)$$

is useful to measure the strength of correlations. At the Fermi-point and at a fixed temperature T , it varies from $-\frac{1}{2}$ for $U = 0$, an uncorrelated system, to 0 for $U = \infty$, a highly-correlated system. In Fig. 4(a), 5(a), and 6(a), we display $G(\tau)$ for $U = 2, 4, 6$; $N_c = 4, 8, 16$; and $\beta = 5$ for FSS and for the DCA. These parameters were chosen to illustrate the three situations that are

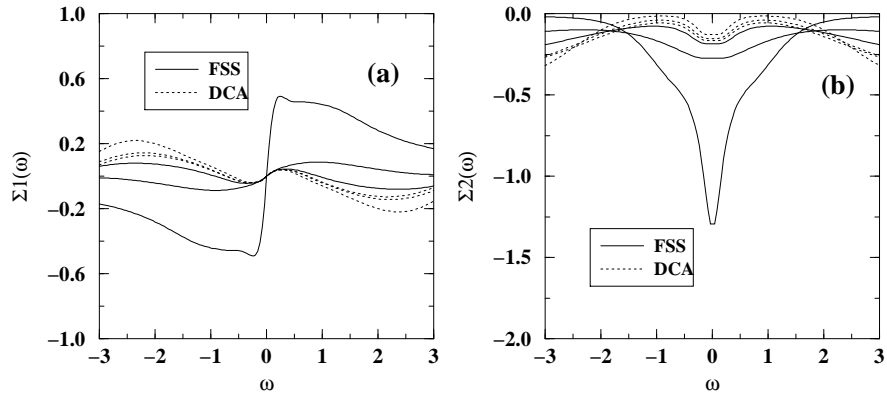


Fig. 7. Real (a) and Imaginary (b) part of Σ at the Fermi point for $U = 2$, $\beta = 5$ for FSS (solid lines) for $N_c=4,8,16$ and for DCA (dotted lines).

generic in the model: the metallic, the pseudogap, and the insulating regimes, respectively. In all cases, $G(k_F, \beta/2)$ decreases with increasing cluster size for FSS while for the DCA it increases.

This behavior marks the fundamental difference between FSS and the DCA. At low temperatures, in FSS, the correlation length is greater than the lattice size. Thus, the effects of correlations are overestimated for smaller clusters because the systems are artificially closer to criticality than a system in the thermodynamic limit. This tendency is reduced by increasing the cluster size, which moves the system in the direction of the thermodynamic limit. The situation is radically different in the DCA where the system is already in the thermodynamic limit. The DCA approximation restricts correlations to within the cluster length. As the cluster size increases, longer range correlations are progressively included. Thus, the effects of the correlations increase with the size of the cluster.

This analysis is supported by the spectra shown in Fig. 4(b), 5(b), and 6(b). For $U = 2$, FSS shows a pseudogap for $N_c = 4$. This pseudogap vanishes at $N_c = 8, 16$ to become a peak at $\omega = 0$. The peak corresponding to $N_c = 16$ is sharper than that of $N_c = 8$. In contrast, the DCA starts with a sharp peak at $N_c = 4$. This peak progressively broadens as N_c is increased to 8 and 16. The FSS and the DCA peaks seem to converge to the same limit consistent with the results of $G(\tau)$. For $U = 4$, the system presents a pseudogap. The convergence to this pseudogap is in conformity with the above analysis. The FSS system goes from a gap to a pseudogap when N_c is increased from 4 to 16. The DCA evolves from a central peak at $N_c = 4$ to a pseudogap at $N_c = 16$. When $U = 6$, the system is gapped; the FSS shows a large gap at $N_c = 4$. This gap decreases for $N_c = 8$ and $N_c = 16$.

In Fig. 7(a), 8(a), and 9(a), we show the real part of the self energy at $\beta = 5$ for various interaction strengths, U . For $U = 2$ (Fig. 7), where a

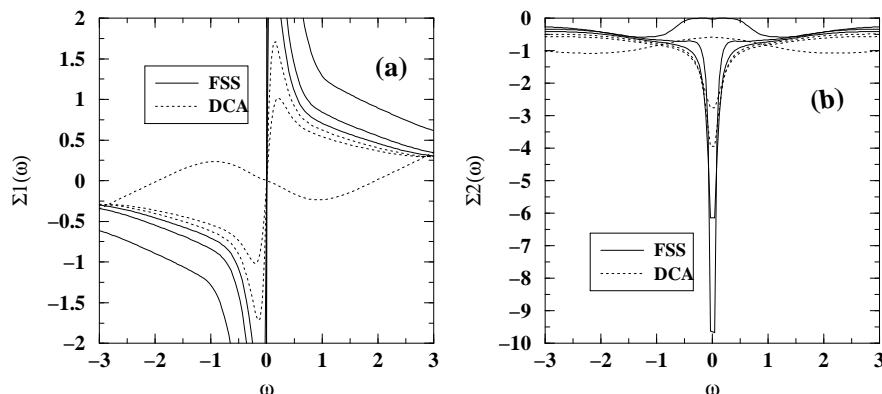


Fig. 8. Real (a) and Imaginary (b) part of Σ at the Fermi point for $U = 4$, $\beta = 5$ for FSS (solid lines) for $N_c=4,8,16$ and for DCA (dotted lines).

pseudogap exists for $N_c = 4$, Σ_1 via FSS has two solutions at non-zero ω for the equation $\omega - \epsilon_k - \Sigma_1(\omega) = 0$. This happens when the slope $\frac{dRe\Sigma(\omega)}{d\omega}$ is greater than unity. This derivative decreases and becomes smaller than 1 for $N_c = 8, 16$ corresponding to the single peak in $A(\omega)$. In the DCA, $\frac{dRe\Sigma(\omega)}{d\omega}$ slowly increases with N_c but always remains smaller than 1.

The Imaginary part of the self energy $\Sigma_2(\omega)$ shown in Fig. 7(b), 8(b), and 9(b), also has a monotonic behavior in which the limiting value is bracketed by FSS and DCA results. A general trend that emerges is that $\Sigma_2(\omega)$ has a local minimum in the vicinity of $\omega = 0$ in the metallic regime (Fig. 7), which minimum deepens sharply when a pseudogap appears (Fig. 8), and finally $\Sigma_2(\omega = 0)$ vanishes in the insulating regime (Fig. 9).

6 Summary

We have extensively analyzed the DCA by comparing it to FSS. A coherent picture emerges from the investigation of the single-particle properties of the 1D Hubbard model. By systematically underestimating the effects of correlations, the DCA converges to the limiting value of a given quantity from a starting point that is opposite to the starting point of FSS. Thus, the DCA can help resolve situations where one is unable to draw a conclusion from FSS alone. For example, in spite of considerable work with FSS, it has not been possible to make a definitive statement as to the existence of a pseudogap in the weak-coupling (U smaller than the band-width) regime of the two-dimensional Hubbard model at half-filling. It was impossible to get a definite answer from FSS because, as expected, the pseudogap seemed to vanish when the cluster size was increased [14]. Recently, using DCA, Huscroft et al. showed that there is a pseudogap for 4×4 to 8×8 clusters [15]. From the

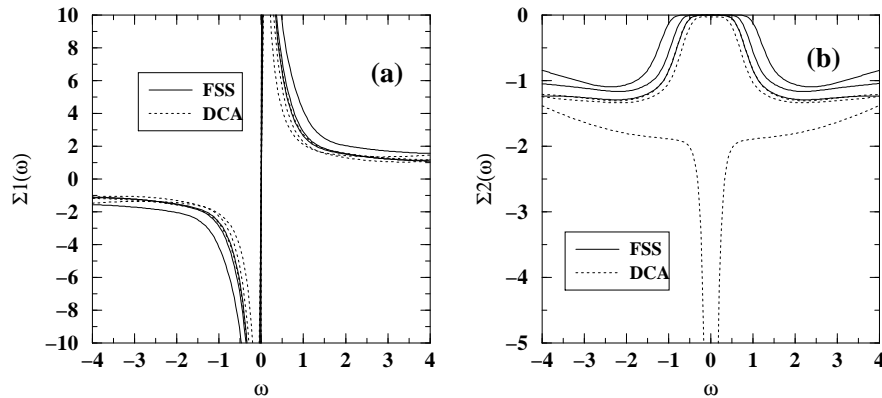


Fig. 9. Real (a) and Imaginary (b) part of Σ at the Fermi point for $U = 6$, $\beta = 5$ for FSS (solid lines) for $N_c=4,8,16$ and for DCA (dotted line).

analysis above, since the DCA underestimates the effects of correlations, this demonstrates unambiguously the existence of the pseudogap in the half-filled Hubbard Model in the thermodynamic limit.

The DCA has shown great promise and, even though a young method, has already illustrated its great utility. Still, much work remains to be done. One immediate application is the the nature of the ground state of the two dimensional Hubbard model; is it a Mott insulator or antiferromagnetic (Slater) insulator? Another is the problem raised by Anderson concerning the low energy behavior of 2D coupled doped Hubbard chains; are they Luttinger or Fermi liquids? [16] Both of these problems have proven difficult to tackle using FSS approaches alone. Finally, we have not discussed the convergence of the two-particle quantities. A systematic comparison with FSS as in this work will be the subject of a future study.

Acknowledgments: We wish to thank S. Allen for sharing his BSS data. This work was supported by NSF grants DMR-9704021, DMR-9357199 and by the Ohio Supercomputer Center.

References

1. E. Dagotto: Rev. Mod. Phys. **66**, 763 (1994)
2. M.H. Hettler *et al.*: Phys. Rev. **B 58**, 7475 (1998)
3. M.H. Hettler *et al.*: preprint cond-mat/9903273
4. Th. Maier *et al.*: Eur. Phys. J. *to appear* (1999)
5. W. Metzner and D. Vollhardt: Phys. Rev. Lett. **62**, 324 (1989)
6. D.F. Elliot and K.R. Rao, *Fast Transforms: Algorithms, Analyses, Applications* (Academic Press, New York, 1982)
7. E. Müller-Hartmann: Z. Phys. **B 74**, 507–512 (1989)
8. J.E. Hirsch and R.M. Fye: Phys. Rev. Lett. **56**, 2521 (1986)
9. M. Jarrell and J.E. Gubernatis: Phys. Rep. **269**, 135 (1996)
10. M. Jarrell, H. Akhlaghpour and T. Prushke: Quantum Monte Carlo Methods in Condensed Matter Physics, Eds M. Suzuki (World Scientific, p. 221–234, 1993)
11. R. Blankenbecler, D.J. Scalapino, and R.L. Sugar: Phys. Rev. **D 24**, 2278 (1981)
12. A. Georges, G. Kotliar, W. Krauth and M.J. Rozenberg: Rev. Mod. Phys. **68**, 13 (1996)
13. T. Pruschke, M. Jarrell and J.K. Freericks: Adv. in Phys. **42**, 187 (1995)
14. M. Vekic and S.R. White: Phys. Rev. **B 47**, 1160 (1993)
15. C. Huscroft *et al.*: preprint cond-mat/9910226
16. P.W. Anderson: Phys. Rev. Lett. **64**, 1839 (1990); **65**, 2306 (1990)